Supplementary Materials for

Electrically Pumped Terahertz Frequency Comb Based on Actively Mode-locked Resonant Tunneling Diode

Feifan Han[1]†, Xiongbin Yu[1]†*, Qun Zhang[1], Zebin Huang[1], Longhao Zou[1], Weichao Li[1], Jingpu Duan[1], Zhen Gao[4]*, Xiaofeng Tao[2,1]* and Ping Zhang[3]*

[1]Department of Broadband Communication, Pengcheng Laboratory, Shenzhen 518057, China.

[2]National Engineering Research Center of Mobile Network Technologies, Beijing University of Posts and Telecommunications, Beijing 100876, China.

[3]State Key Laboratory of Network and Switching Technology, Beijing University of Posts and Telecommunications, Beijing 100876, China.

[4]State Key Laboratory of Optical Fiber and Cable Manufacture Technology, Department of Electronic and Electrical Engineering, Guangdong Key Laboratory of Integrated Optoelectronics Intellisense, Southern University of Science and Technology, Shenzhen 518055, China.

†These authors contributed equally to this work.

*Corresponding author. Email: yuxb@pcl.ac.cn (X.B.Y.); gaoz@sustech.edu.cn (Z.G.); taoxf@bupt.edu.cn (X.F.T.), pzhang@bupt.edu.cn (P.Z.)

This PDF file includes:

Supplementary Note 1-7

Figs. S1-11

Tables. S1-S2

References

Note 1. Coupling between RTD and WR-5 waveguide.

To investigate the mechanism of TFC extracted from the RTD oscillator coupled into the WR-5 waveguide, we performed a three-dimensional (3D) electromagnetic simulation. In the simulation, we placed a wave port at the end of the waveguide and replaced the RTD with a lumped port, as shown in Fig. S1a-b. Fig. S1c showed the calculated transmission coefficient S_{21} and the coupling efficiency. The coupling efficiency is defined as

$$\eta = \frac{|S_{21}|^2}{1 - |S_{11}|^2} \tag{1}$$

, which represents the power extracted from the RTD oscillator and coupled into the waveguide. The simulation indicates a coupling efficiency of approximately 40% near 0.18 THz, resulting from relative effective impedance matching between the RTD oscillator and the waveguide. Conversely, a significant impedance mismatch occurs around 0.19 THz, leading to poor coupling. This is the primary reason for the degradation of the measured TFC power at frequencies above 0.19 THz. Fig. S1d-f and Fig. S1g-i illustrate the simulated electric field (E-field) distributions in the x-z, x-y, and y-z planes for the RTD oscillator inside the waveguide (Fig. S1d-f) and the RTD oscillator itself (Fig. S1g-i), respectively. The intense E-field generated by the RTD oscillator couples into the waveguide primarily through the long part of the slot resonator. The E-field leaked from the short part of the slot resonator propagates to the left-hand end of the waveguide, located 0.8 mm from the RTD chip. This waveguide end functions as a metal reflector, causing the reflected wave to travel back in the right-hand direction. The reflected wave also travels in the right-hand direction. The presence of a traveling wave propagating along the waveguide confirms the effective extraction of the TFC power from the RTD oscillator to the waveguide. A magnified view of the E-field in the vicinity of the RTD oscillator reveals a strong field concentration, indicating the resonant behavior of the slot and split-ring resonators.

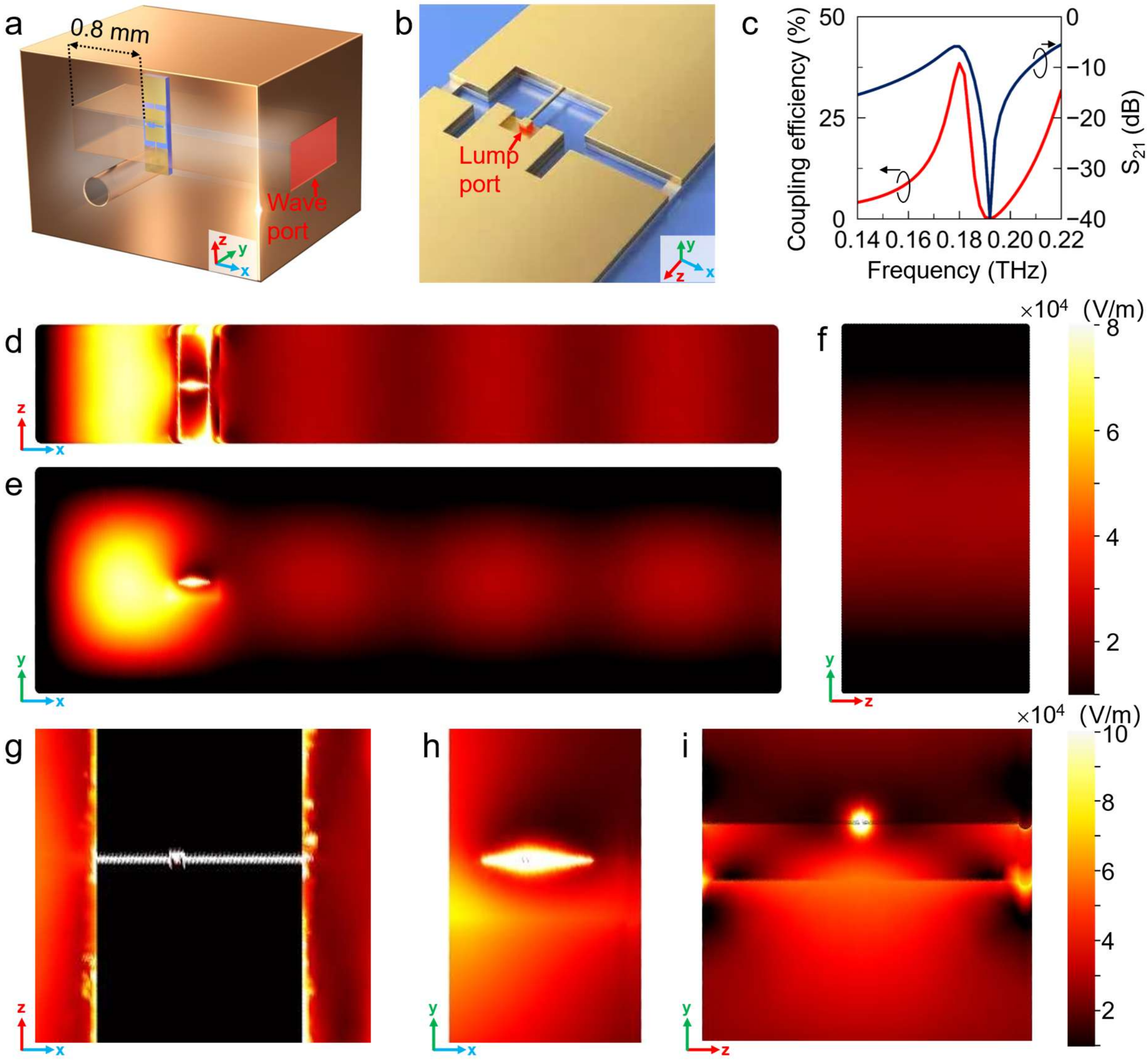

Fig. S1 | Electromagnetic simulations of the RTD in a metallic waveguide. a, Configuration of the wave port at the waveguide output. **b,** Lumped port assignment representing the RTD element. **c,** Calculated coupling efficiency and transmission coefficient S_{21}. **d-e,** Simulated electric field distributions in the x-z and x-y planes, respectively, illustrate the extraction of the electromagnetic wave from the RTD chip into the waveguide. **f,** Simulated electric field distribution in the y-z plane showing one of the wave crests inside the waveguide. **g-i,** Magnified electric field distributions in the x-z, x-y, and y-z planes of the RTD oscillator itself, respectively, indicate strong resonance and field confinement within the slot and split-ring resonators.

Note 2. Packaging

The WR-5 waveguide package was fabricated by Computer Numerical Control (CNC) milling in two parts. As shown in Fig. 2b, the RTD chip is mounted inside the upper half of the package. The magnified microscope picture showing the details of the RTD chip packaged to the waveguide is shown in Fig. S2. A 1.85-mm RF coaxial connector is inserted through a hole positioned near the chip location, appearing as the inner conductor of the connector in Fig. S2. After fixing the connector with two screws, it shares a common ground with the waveguide package.

The RTD chip was polished from 600 to 100 μm and diced into 300×900 μm dies. To mount the RTD, a small amount of wax was first dipped into the mounting hole. After cooling, the RTD chip was placed on the wax using tweezers. The wax was then reheated and cooled again to firmly attach the chip to the package. Wire bonding was carried out to connect the inner conductor of the connector to the RTD. A second bonding wire was taken directly from the waveguide package to the RTD. Since the package and connector share the same ground, this configuration allows both DC biasing and RF signal injection through the connector.

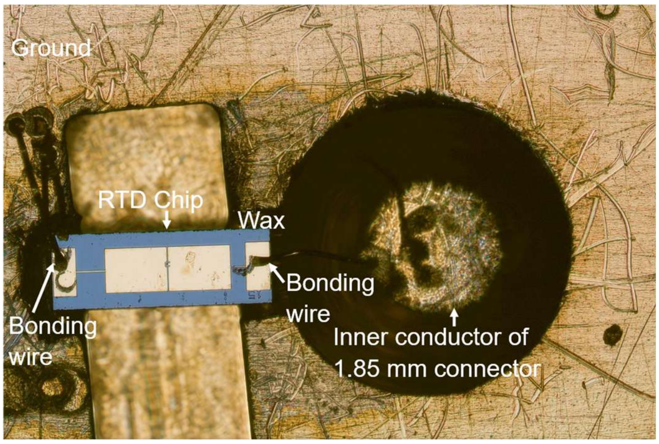

Fig. S2 | Detailed RTD packaging method. The RTD chip is fixed within the WR-5 waveguide using wax. The inner conductor of a 1.85 mm coaxial connector is inserted through a cylindrical hole and positioned in close proximity to the RTD chip. We connected two bonding wires to the RTD chip. The right wire is connected to the inner conductor of the coaxial connector to establish the signal path. The left wire is directly connected to the package, serving as the signal ground.

Note 3. Fabrication process.

Figure S3 depicts the detailed geometrical parameters of the RTD oscillator and the epitaxial layer structure of the RTD wafer. The short slot, long slot, and perimeter of the split ring are 60, 100, and 60 μm, respectively. The split ring enhances the concentration of the electric field within the slot resonator, thereby reducing losses[1]. The incorporation of the Al element into the InGaAs layer, grown on the n^+InP layer, results in a reduction of the conduction band energy level on the emitter side of the RTD[2]. This design allows the device to enter the negative differential conductance (NDC) region at a low bias voltage. The 10 nm n^+-InP layer serves as an etch stop layer[3] during the wet etching process for the subsequent fabrication steps. Figure S4 describes the fabrication process of the RTD device. A double-layer resist consisting of LOR-2A and PMGI was coated, and photolithography was employed to define the electrode pattern. After depositing Ti/Pd/Au with a thickness of 20/20/200 nm, we performed the lift-off process to form the electrode. The Ti/Pd/Au provides good ohmic contact with n^+-InGaAs. For the subsequent etching step, we used AZ9260 as the dry etching mask. We applied a gas mixture of BCl_3:Cl_2:Ar = 15:5:8 for the ICP-RIE process to remove the n^+-InGaAs inside the slot and outside the DC pads. The shunt resistors were thereby formed, and different RTD elements were isolated. RZJ304-10 was then employed as a protection mask for the wet-etching process used to form the air bridge. Due to the isotropic etching with etchant (H_3PO_4:H_2O_2:H_2O = 1:1:80), the n^+-InGaAs beneath the air bridge was removed laterally, resulting in the formation of the suspended air bridge. After removing the RZJ304-10 protection mask, a final wet-etching step was carried out to remove the semiconductor material near the RTD electrodes, thereby forming the target RTD mesa.

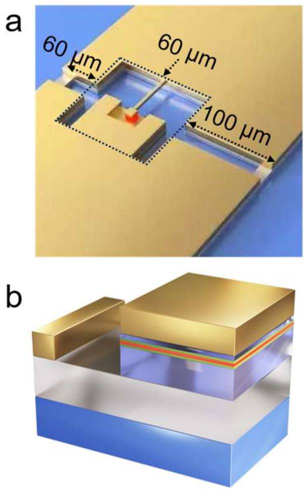

c

n^+- In$_{.9}$Ga$_{.1}$As	3 nm (~5x10^{19}cm^{-3})
n^+-In$_{.53}$Ga$_{.47}$As	15 nm (~5x10^{19}cm^{-3})
un-In$_{.53}$Ga$_{.47}$As	Spacer: 12 nm
AlAs	Barrier: 1.2 nm
un-In$_{.9}$Ga$_{.1}$As	Well: 3 nm
AlAs	Barrier: 1.2 nm
un-In$_{.53}$Al$_{.1}$Ga$_{.37}$As	Spacer: 5 nm
n^+-In$_{.53}$Al$_{.1}$Ga$_{.37}$As	20 nm (~3x10^{18}cm^{-3})
n^+-In$_{.53}$Al$_{.1}$Ga$_{.37}$As	5 nm (~5x10^{19}cm^{-3})
n^+-InP	10 nm (~5x10^{19}cm^{-3})
n^+-In$_{.53}$Ga$_{.47}$As	300 nm (~5x10^{19}cm^{-3})
SI-InP Sub.	600 μm

Fig. S3 | Detailed RTD resonator structure. a, RTD oscillator composed of an active region and a resonator. The short slot, long slot, and perimeter of the split ring are 60, 100, and 60 μm, respectively. **b,** RTD active region in the vertical direction. **c,** Detailed epitaxy layer of RTD.

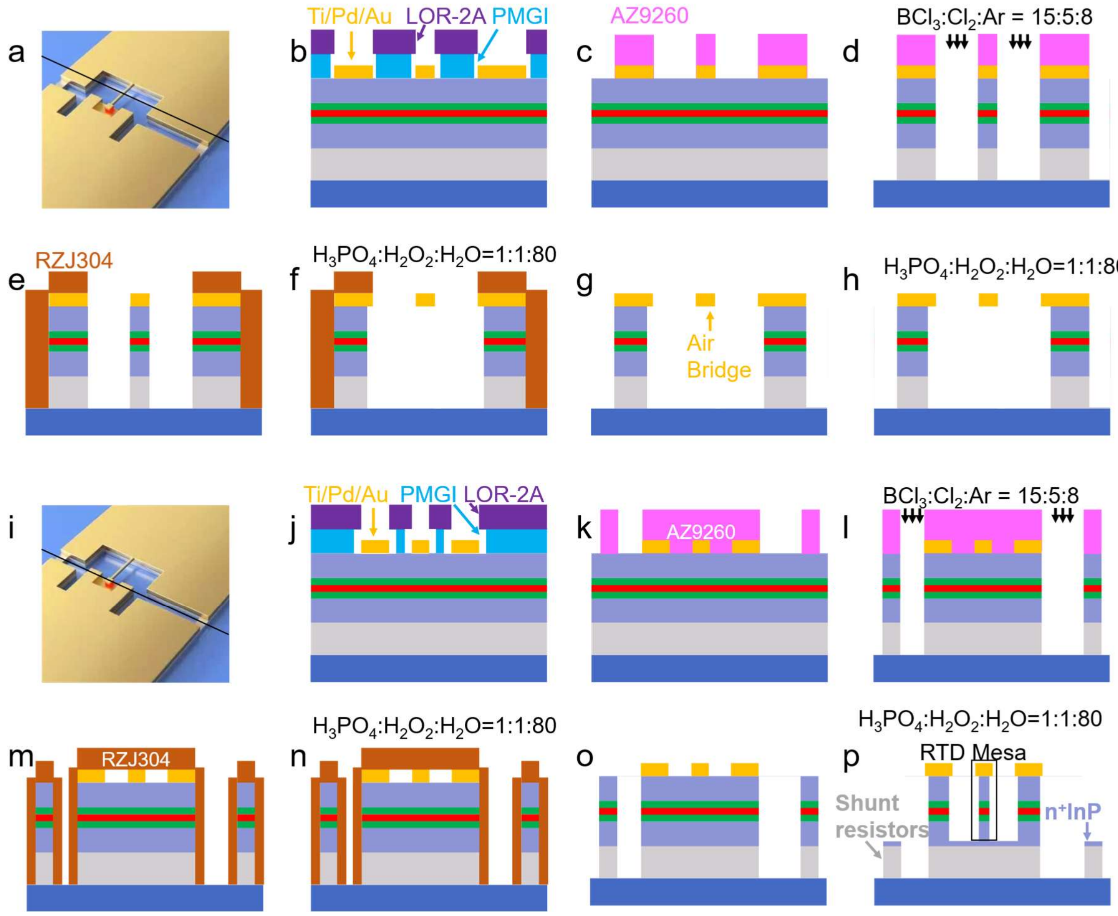

Fig. S4 | Detailed fabrication process. a, Cross-section of air bridge. **b,** LOR-2A and PMGI double layer lithography, and deposition of Ti/Pd/Au = 20/20/200 nm. **c,** AZ9260 as a resist mask for ICP-RIE. **d,** Gas mixture of BCl_3:Cl_2:Ar = 15:5:8 for semiconductor dry etching. **e,** RZJ304 is a resist mask for wet etching. **f,** An air bridge is formed using a wet etching process with an etchant (H_3PO_4:H_2O_2:H_2O = 1:1:80). Due to the isotropic direction of this chemical etch, the material layers beneath the metal are removed. This undercutting action results in the formation of the desired air bridge structure. **g,** Removal of RZJ304. **h,** Extra wet etching. **i,** Cross-section of RTD mesa and shunt resistors. **j,** LOR-2A and PMGI double-layer lithography, and deposition of Ti/Pd/Au = 20/20/200 nm. **k,** AZ9260 is a resist mask for ICP-RIE. **l,** Gas mixture of BCl_3:Cl_2:Ar = 15:5:8 for semiconductor dry etching. The shape of the shunt resistors was formed. **m,** RZJ304 as a resist mask for wet etching. **n,** The RTD part and the shunt resistors were protected from over-etching. **o,** Removal of RZJ304. **p,** An additional wet etching step is performed to fabricate the RTD mesa and the shunt resistors. The duration of this etch is precisely controlled to define the RTD mesa and achieve the target area. The etching process selectively stops at the n^+InP layer, which serves as an etch-stop and enables the formation of the shunt resistors.

Note 4. Circuit simulation.

We modeled the RTD oscillator under TFC conditions using the equivalent circuit shown in Fig. S5a. TFC generation requires strong RF injection, which we represent as an RF source with a 50 Ω source impedance. The source is in parallel with RTD, and its power is represented as P_{RF}. The oscillator circuit includes the RTD in parallel with its resonator load, a simplified model derived from the structure in Fig. 2c, radiation resistance R_{rad}, and resonators' parasitic capacitance C_p. The equivalent resonator resistance R_{load}, resonator inductance L_{load}, R_{rad}, and C_p are approximately 12.7 Ω, 31.4 pH, 460 Ω, and 5.8 fF, respectively. The RTD area S_{RTD} is 2.7 μm^2. We modeled the RTD with a linear capacitance $C_{RTD} = S_{RTD} \times 11$ fF/μm^2, and a nonlinear voltage-dependent conductance $G_{RTD}(V) = I_{RTD}(V)/V$. To extract the RTD current $I_{RTD}(V)$, we performed DC measurements of RTD. In the DC measurement setup (Fig. S5b), parasitic components, including a shunt resistor ($R_{shunt} \approx 9$ Ω) and series resistance ($R_{series} \approx 15$ Ω) from the bias tee, obscure the intrinsic RTD characteristics. Consequently, the measured NDC region shifted to ~1.9–2.6 V (Fig. S5d, blue line). To extract the *I-V* characteristics required for the high-frequency simulation in Fig. S5a, we fabricated and measured a separate RTD device lacking the R_{shunt} and R_{series}. The test setup in Fig. S5c minimizes parasitic resistances and provides a relatively accurate intrinsic *I-V* curve, as shown in Fig. S5d (red line), revealing the NDC region between ~0.6 V and 1.1 V. The nonlinear current $I_{RTD}(V)$ used in the model was subsequently derived as[4,5]:

$$I_{RTD}(V) = S_{RTD}\left(C_1 V\{\tan^{-1} C_2(V - V_1) - \tan^{-1} C_2(V - V_2)\} + C_3 V^i\right) \quad (2)$$

The parameters of Equation 2 are shown in Table S1. We simulated the TFC circuit using the harmonic balance method with $f_{RF} = 0.918$ GHz, $P_{RF} = 10$ dBm, and 0.7 V bias. Taking the voltage across R_{rad} as the output, we observed the TFC generation and the corresponding spectrum as presented in Fig. 2h.

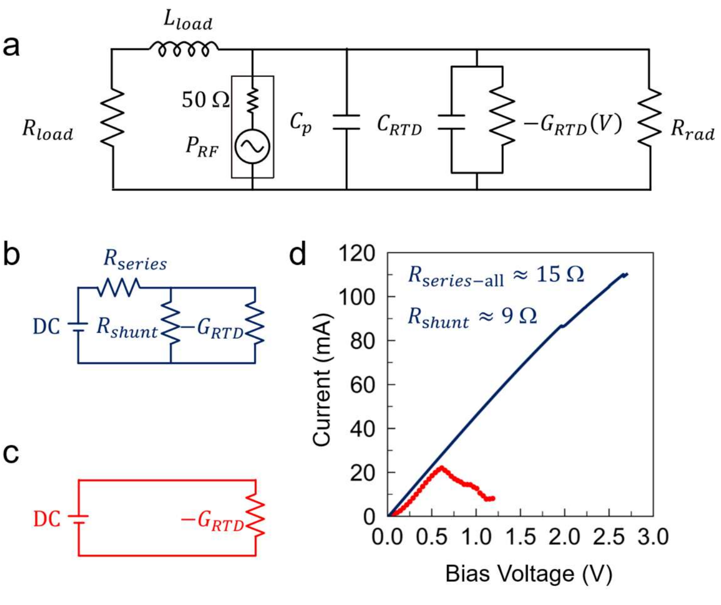

Fig. S5 | Circuit diagram in simulation and *I-V* characteristics. a, Equivalent circuit diagram of the RTD model used for simulation. RTD is connected in parallel with an RF source having an internal resistance of 50 Ω, a resonator load, parasitic capacitance, and radiation resistance. **b,** DC circuit diagram of RTD with shunt resistors and series resistors from the bias tee. **c,** DC circuit diagram of RTD without a shunt resistor and series resistors from the bias tee. **d,** Comparison of measured RTD *I-V* curve with and without shunt resistors and series resistor

Function	Parameter	Value	Unit
$I_{RTD}(V)$	S_{RTD}	2.7	μm^2
	C_1	0.03	$A \cdot V^{-1} \cdot \mu m^{-2}$
	C_2	5.5	V^{-1}
	V_1	0.62	V
	V_2	0.24	V
	C_3	0.0015	$A \cdot V^{-i} \cdot \mu m^{-2}$
	i	5.4	$-$

Table S1 | Parameters of $I_{RTD}(V)$

Note 5. Output power measurement.

To characterize the output power of the RTD oscillator, we connected the module to an Erickson PM5 power meter through a WR-5 waveguide, as shown in Fig. S6. In its free-running state at 0.188 THz, the module was −12 dBm. A THz LNA then amplified this signal to 1.3 dBm. To induce TFC operation, we injected a 20 GHz, 13 dBm RF signal. The module's output power was −19.1 dBm, and it was amplified by the THz LNA to −2.5 dBm.

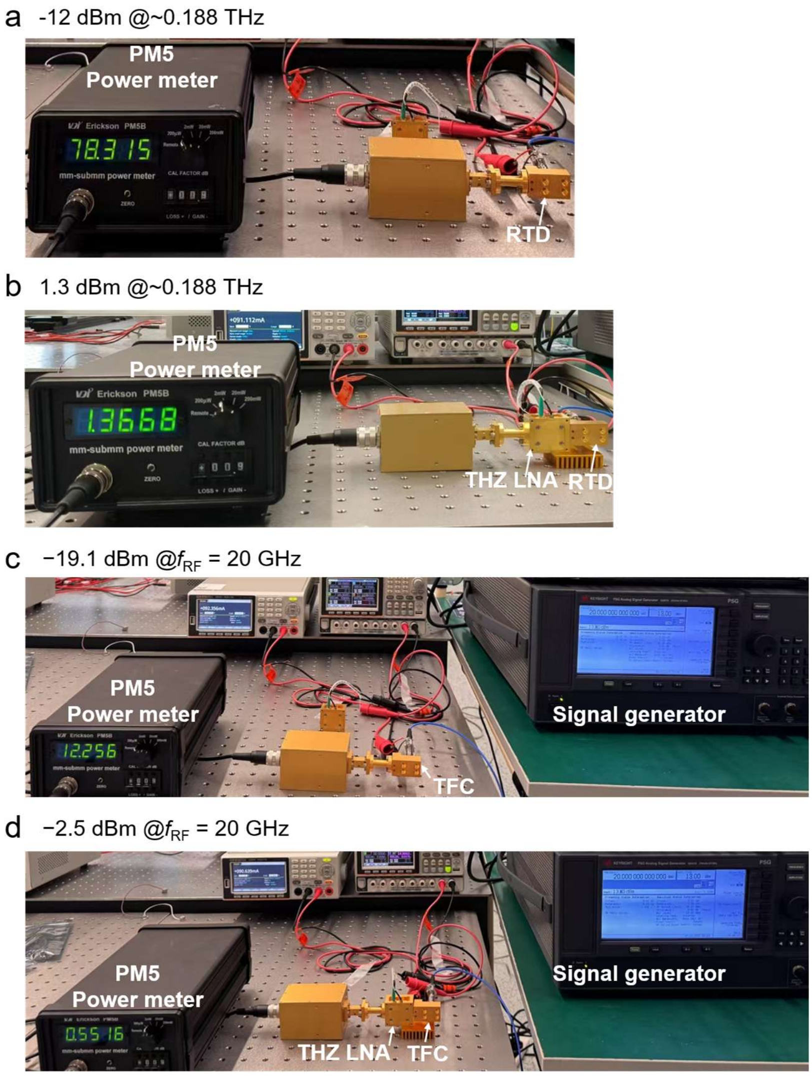

Fig. S6 | Output power measurement. a, Power measurement of free-running RTD. **b,** Power measurement of free-running RTD with THz LNA. **c,** Power measurement of RTD TFC under 20 GHz 13 dBm injection. **d,** Power measurement of RTD TFC under 20 GHz 13 dBm injection with THz LNA.

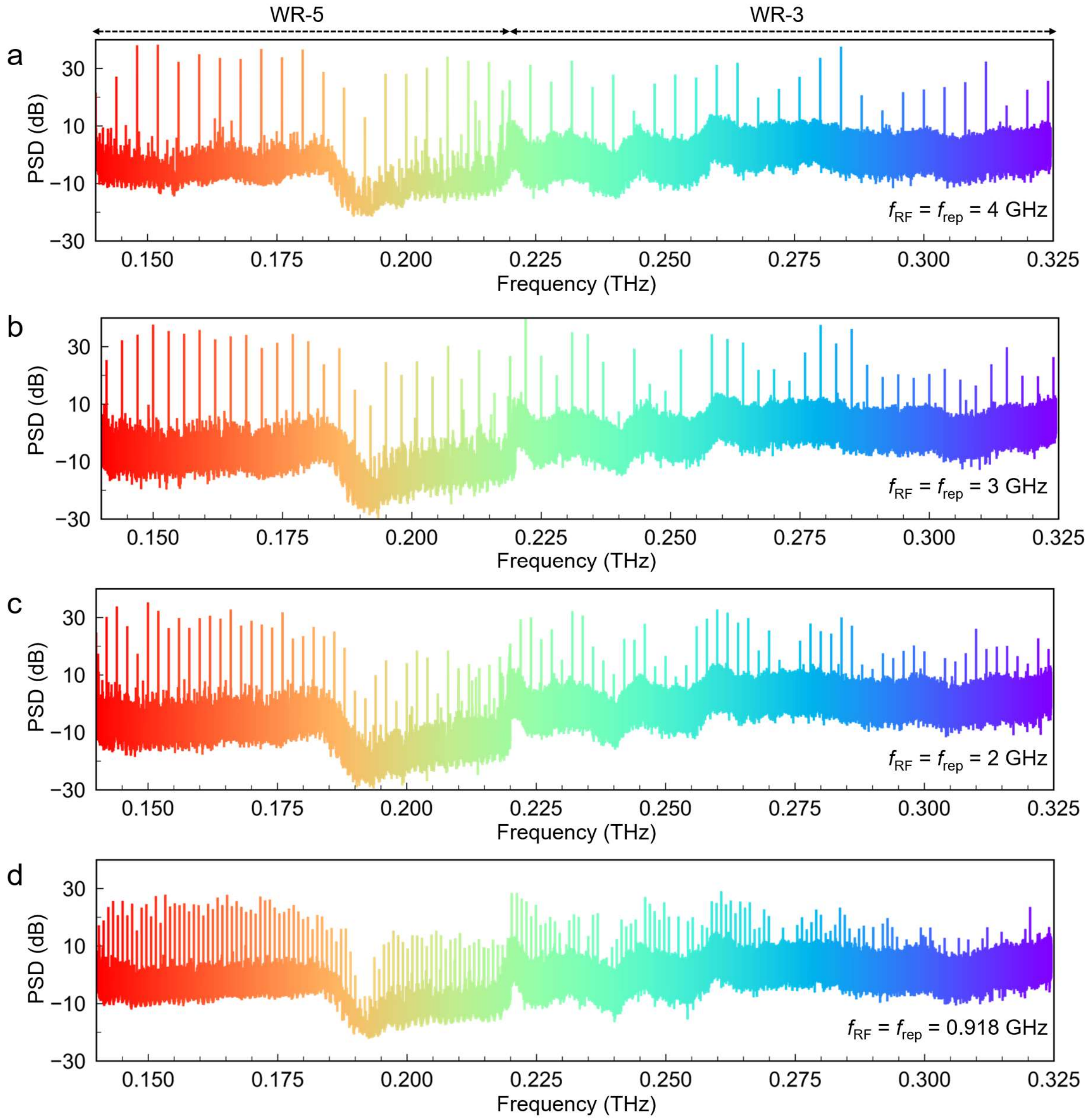

Fig. S7 | Measured spectra of TFC with different RF frequencies and fixed RF injection power of 18 dBm. a, f_{RF} = 0.918 GHz, **b,** f_{RF} = 2 GHz, **c,** f_{RF} = 3 GHz, and **d,** f_{RF} = 4 GHz. The measurements were performed using two different frequency extenders (WR-5 & WR-3 waveguide types) to cover the spectral ranges of 0.14–0.22 THz and 0.22–0.325 THz. Notably, comb modes are observed at frequencies exceeding 0.3 THz, which is significantly higher than the fundamental frequency of the RTD oscillator. This result highlights the potential for generating TFCs at frequencies far beyond the device's fundamental mode. Furthermore, the ability to generate a stable TFC at different repetition frequencies demonstrates that the comb is widely tunable through the active mode-locking mechanism.

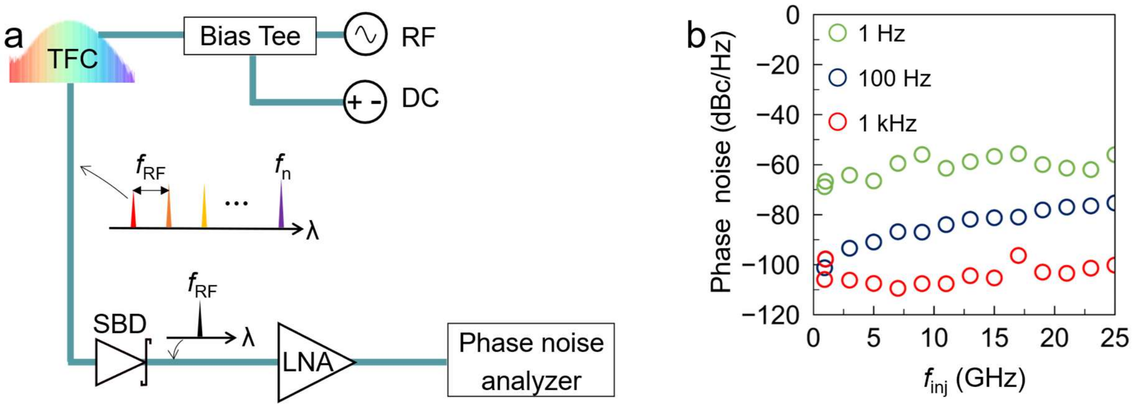

Fig. S8 | Phase noise measurement. a, Schematic of the TFC Phase noise measurement setup. The beat note, namely f_{RF}, is detected at SBD and transmitted to the phase noise analyzer. **b,** Measured phase noise dependence on f_{RF} at 1 Hz, 100 Hz, and 1 kHz, respectively.

Note 6. Sweeping bias voltage and f_{RF}.

To determine the conditions required for active mode-locking under RF injection, the RTD bias voltage and the injected RF power were systematically varied. The bias voltage was swept from 1.3 to 2.7 V, a range that encompasses the device's NDC region, which spans ~1.9–2.7 V. To prevent device breakdown, measurements were not conducted beyond this upper voltage limit. The device's operation can be roughly classified into free-running, modulation, unstable free-running, unstable comb, and comb states. These states are labeled in Fig. S9b when f_{RF} is 20 GHz. We neglect the free-running state because it does not exist when an RF signal is injected. We also neglect the unstable comb state because it is a transition state that only exists within the change of ~1–2 dBm. To visualize these operational regimes, the spectral power at 0.14, 0.16, 0.18, 0.2, and 0.22 THz was summed, with the total power plotted in Fig. S9a. A low summed power is characteristic of the unstable free-running state, where modulation and comb states coexist (blue and cyan areas). A high summed power indicates stable comb generation (red and orange areas). Notably, comb states were observed at bias voltages far below the beginning of the NDC region. This is attributed to the large-signal RF injection, which induces a voltage swing sufficient to drive the RTD instantaneously into the NDC region. Furthermore, the strong power observed at the beginning of the NDC region is likely due to the pronounced nonlinearity of the device at that bias point.

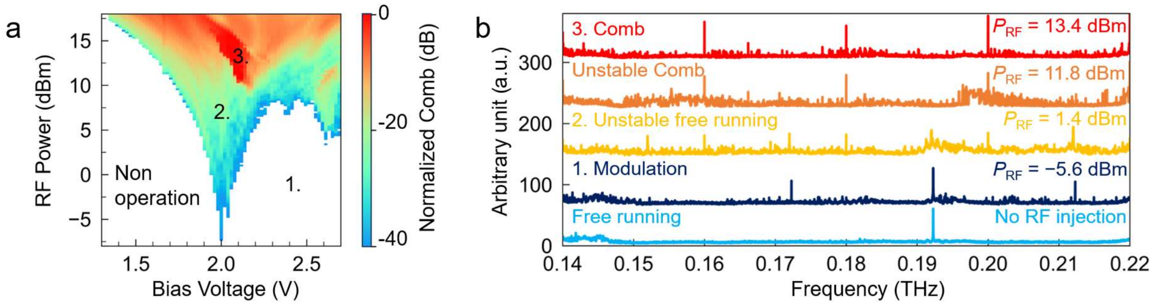

Fig. S9 | Phase diagram of the measured comb power as a function of RF injection power and bias voltage. a, Total comb power at 0.14, 0.16, 0.18, 0.20, and 0.22 THz when f_{RF} = 20 GHz. **b,** Different operation conditions with different RF power.

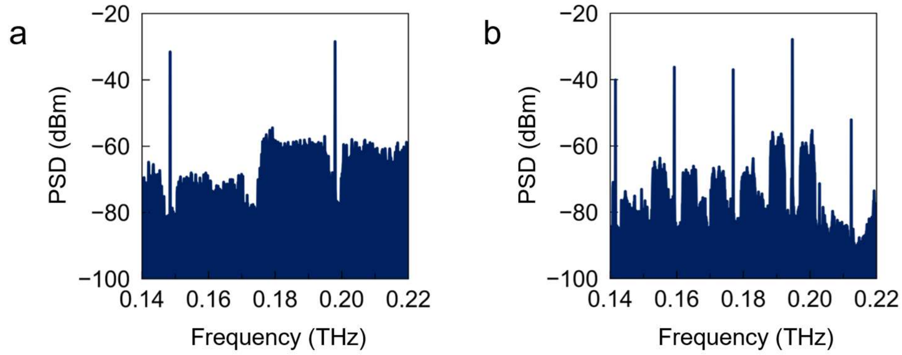

Fig. S10 | Transmitted signal spectrum in wireless communication. a, Single channel with 32-QAM 24 Gbaud communication when f_{RF} = 49.5 and f_5 = 0.198 THz. **b,** Three-channel with 16-QAM 4 Gbaud communication when f_{RF} = 17.7 GHz and f_9 = 0.159, f_{10} = 0.177, and f_{11} = 0.195 THz.

Note 7. Digital signal processing.

The single-carrier (SC) modulation is implemented in our experimental systems, which is considered a spectral- and energy-efficient technology for THz wireless communications. The main offline DSP flows are shown in Fig. S11. At the Tx DSP module, SC-16QAM/32QAM signals are generated with randomly chosen symbol sequences of length 2^{16} and up-sampled at 2 samples per symbol. Subsequently, a raised-cosine (RC) filter with a roll-off factor of 0.1 is implemented for the pulse shaping. These shaping signals, after undergoing digital up-conversion (DUC) and resampling, are used to drive the mixer. At the Rx DSP module, received signals are initially processed by digital down-conversion (DDC) to obtain baseband signals and then passed through a low-pass filter to eliminate out-of-band noise. Following this, a series of advanced DSP modules, including timing phase recovery, linear/nonlinear channel equalization, and noise cancellation, are implemented to enhance the system performance. The details of the above algorithms are as follows:

The timing phase recovery based on Godard timing error detection (TED)[7] is applied to mitigate sampling frequency/phase errors, which is a popular frequency domain TED algorithm widely used in SC communication systems. The principle of Godard TED can be expressed as

$$\tau(k) = \frac{angle\left(\sum_{n=(k-1)N+1}^{(k-1)N+\frac{N}{2}} S\,(n) S^{*}\left(n+\frac{N}{2}\right)\right)}{2\pi f_s} \tag{3}$$

where τ represents the timing error, k represents the block index, N represents the length of the fast Fourier transform (FFT) block, S represents the FFT of the input signals, f_s represents the sample rate, and $angle$ represents the operation of measuring an angle.

The linear channel equalization based on a T/2-spaced radius-direction equalizer (RDE)[8] is implemented to mitigate inter-symbol interference (ISI), which typically results from multipath propagation, non-flat channel frequency responses, and standing wave effects. RDE is a kind of adaptive filtering algorithm with the mean square error of power as the cost function. The advantage of RDE is insensitive to carrier frequency and phase errors, which is conducive to modular programming. The implementation processes of the algorithm are as follows

$$s_{out}(n) = \boldsymbol{w}^{\mathrm{H}} \boldsymbol{s_{in}}(n) \tag{4}$$

$$\boldsymbol{w}(n+1) = \boldsymbol{w}(n) + \mu e(n) s_{out}^{*}(n) \boldsymbol{s_{in}}(n) \tag{5}$$

$$e(n) = |\hat{s}_{out}(n)|^2 - |s_{out}(n)|^2 \tag{6}$$

where s_{out} and $\hat{s}_{out}$ represent the output signal and the related ideal symbol, $\boldsymbol{s_{in}}$ represents the input signal vector of $1 \times \mathrm{N}$, $\boldsymbol{w}$ represents the tap vector of $1 \times \mathrm{N}$, μ represents the step of update, e represents the error function, the superscript '$*$' and 'H' represent conjugate and conjugate transpose operation. Notably, N is set to 151 in this paper, which is sufficiently long to eliminate most of the ISIs.

The nonlinear channel equalization based on T-spaced 2×2 Volterra equalizer (VE)[9] is used to compensate nonlinear distortion, phase noises and residual ISIs. The classic adaptive Volterra equalization algorithm is combined with multiple input multiple output (MIMO) architecture to deal with the nonlinear effects of inter- and intra in-phase/quadrature (IQ) channel. The core equation of 2×2 VE is as follows

$$s_{out,I}(n) = \sum_{k=1}^{K} \sum_{q_1=0}^{N} \dots \sum_{q_k=0}^{N} w_{II}\left(q_1, \dots, q_k\right) \prod_{m=1}^{k} s_{in,I}(n - q_m) + \sum_{k=1}^{K} \sum_{q_1=0}^{N} \dots \sum_{q_k=0}^{N} w_{QI}\left(q_1, \dots, q_k\right) \prod_{m=1}^{k} s_{in,Q}(n - q_m) \tag{7}$$

$$s_{out,Q}(n) = \sum_{k=1}^{K} \sum_{q_1=0}^{N} \dots \sum_{q_k=0}^{N} w_{IQ}\left(q_1, \dots, q_k\right) \prod_{m=1}^{k} s_{in,I}(n - q_m) + \sum_{k=1}^{K} \sum_{q_1=0}^{N} \dots \sum_{q_k=0}^{N} w_{QQ}\left(q_1, \dots, q_k\right) \prod_{m=1}^{k} s_{in,Q}(n - q_m) \tag{8}$$

where K represents the nonlinear order, N represents the memory length, $w_{II/QI/IQ/QQ}$ represents the tap of MIMO filter, the subscript 'I' and 'Q' represent I and Q parts of the received complex signals. In this paper, a 2×2 third-order Volterra equalizer with a memory length of 6 is applied. Such a short filtering scheme aims to strike a balance between complexity and performance.

Noise cancellation (NC) based on error autocorrelation calculation[10] is implemented to mitigate the amplified colored noise caused by frequency-selective fading. Both pre- and post-cursor noise correlations are considered in the proposed scheme, and the related principle is as follows.

$$s_{out}(n) = s_{in}(n) - \sum_{k=-\frac{N}{2},\ k\neq 0}^{\frac{N}{2}} c_k e(n-k) \tag{8}$$

$$c_k = \frac{\sum_{m=1}^{M-k} e(m) e^*(m+k)}{M-k}, \qquad c_{-k} = c_k^* \tag{9}$$

$$e(n) = \hat{s}_{in}(n) - s_{in}(n) \tag{10}$$

where N is the half-length of NC filter, c_k represents the error autocorrelation parameter, M represents the symbol length used to calculate autocorrelation. N is set to 15 in this paper.

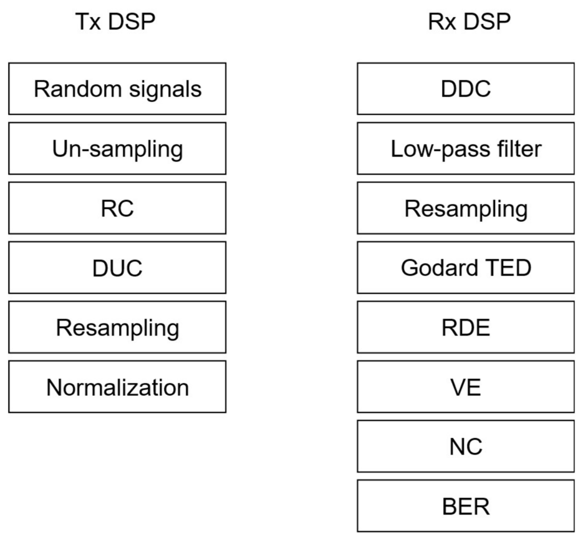

Fig. S11 | DSP flow of Tx and Rx in wireless communication

Technology type	Integration	Pump type	Operation temperature	Comb span (THz)	Repetition rate (GHz)	Phase noise @100 Hz (dBc/Hz)	Linewidth (Hz)	Reference
RTD	**Yes**	**RF**	**Room temperature (R.T.)**	**0.14-0.325**	**0.9-49.5**	**-100**	**1**	**This work**
RTD	No (Quasi-optical external cavity)	No input	R.T.	0.293-0.303	1	N/A	1	4
DFG-QCL	Yes	No input	R.T.	2.2-3.3	157	N/A	N/A	11
QCL	Yes	RF	20 K	2.45-2.55	13.3	N/A	N/A	12
QCL	Yes	No input	< 55 K	1.64-3.35	N/A	N/A	980	13
QCL	Yes	No input	50 K	3.25-3.5, 3.65-3.85	6.8	N/A	1530	14
CMOS	Yes	RF	R.T.	0.22-0.32	10	-50	N/A	15
CMOS &PIN-Diode	Yes	Digital pulse	R.T.	0.03-1.1	15	-50	1	16

Table S2 | Summary of the key metrics of TFC performances.

References

1. Yu, X., Suzuki, Y., Ta, M., Suzuki, S. & Asada, M. Highly efficient resonant tunneling diode terahertz oscillator with a split ring resonator. *IEEE Electron Device Lett.* **42**, 982–985 (2021).
2. Suzuki, S., Asada, M., Teranishi, A., Sugiyama, H. & Yokoyama, H. Fundamental oscillation of resonant tunneling diodes above 1 THz at room temperature. *Appl. Phys. Lett.* **97**, 242102 (2010).
3. Mai, T., Suzuki, Y., Yu, X., Suzuki, S. & Asada, M. Structure-simplified resonant-tunneling-diode terahertz oscillator without metal-insulator-metal capacitors. *J. Infrared Millim. Terahertz Waves* **41**, 1498–1507 (2020).
4. Hiraoka, T., Inose, Y., Arikawa, T., Ito, H. & Tanaka, K. Passive mode-locking and terahertz frequency comb generation in resonant-tunneling-diode oscillator. *Nat. Commun.* **13**, 3740 (2022).
5. Diebold, S. et al. Modeling and simulation of terahertz resonant tunneling diode-based circuits. *IEEE Trans. Terahertz Sci. Technol.* **6**, 716–723 (2016).
6. Sarieddeen, H., Alouini, M. & Al-Naffouri, T. An overview of signal processing techniques for terahertz communications. *Proc. IEEE* **109**, 1628–1665 (2021).
7. Godard, D. Passband timing recovery in an all-digital modem receiver. *IEEE Trans. Commun.* **26**, 517–523 (1978).
8. Zhang, Q. et al. Joint polarization tracking and channel equalization based on radius-directed linear Kalman filter. *Opt. Commun.* **407**, 142–147 (2018).
9. Diamantopoulos, N. et al. On the Complexity reduction of the second-order Volterra nonlinear equalizer for IM/DD systems. *J. Light. Technol.* **37**, 1214–1224 (2019).
10. Wei, J., Stojanovic, N. & Xie, C. Nonlinearity mitigation of intensity modulation and coherent detection systems. *Opt. Lett.* **43**, 3148–3151 (2018).
11. Lu, Q., Wang, F., Wu, D., Slivken, S. & Razeghi, M. Room temperature terahertz semiconductor frequency comb. *Nat. Commun.* **10**, 2403 (2019).
12. Barbieri, S. et al. Coherent sampling of active mode-locked terahertz quantum cascade lasers and frequency synthesis. *Nat. Photon.* **5**, 306–313 (2011).
13. Rösch, M., Scalari, G., Beck, M. & Faist, J. Octave-spanning semiconductor laser. *Nat. Photon.* **9**, 42–47 (2014).
14. Burghoff, D. et al. Terahertz laser frequency combs. *Nat. Photon.* **8**, 462–467 (2014).
15. Wang, C. & Han, R. Rapid and energy-efficient molecular sensing using dual mm-wave combs in 65nm CMOS: A 220-to-320GHz spectrometer with 5.2mW radiated power and 14.6-to-19.5dB noise figure. *IEEE International Solid-State Circuits Conference (ISSCC)*. 302–302 (2017).
16. Razavian, S. & Babakhani, A. Silicon integrated THz comb radiator and receiver for broadband sensing and imaging applications. *IEEE Trans. Microw. Theory Tech.* **69**, 4937–4950 (2021).